LETTER

doi:10.1038/nature20811

Spin–orbit-coupled fermions in an optical lattice clock

S. Kolkowitz[1]*, S. L. Bromley[1]*, T. Bothwell[1], M. L. Wall[1]†, G. E. Marti[1], A. P. Koller[1], X. Zhang[1]†, A. M. Rey[1] & J. Ye[1]

Engineered spin–orbit coupling (SOC) in cold-atom systems can enable the study of new synthetic materials and complex condensed matter phenomena[1–8]. However, spontaneous emission in alkali-atom spin–orbit-coupled systems is hindered by heating, limiting the observation of many-body effects[1,2,5] and motivating research into potential alternatives[9–11]. Here we demonstrate that spin–orbit-coupled fermions can be engineered to occur naturally in a one-dimensional optical lattice clock[12]. In contrast to previous SOC experiments[1–11], here the SOC is both generated and probed using a direct ultra-narrow optical clock transition between two electronic orbital states in ^{87}Sr atoms. We use clock spectroscopy to prepare lattice band populations, internal electronic states and quasi-momenta, and to produce spin–orbit-coupled dynamics. The exceptionally long lifetime of the excited clock state (160 seconds) eliminates decoherence and atom loss from spontaneous emission at all relevant experimental timescales, allowing subsequent momentum- and spin-resolved *in situ* probing of the SOC band structure and eigenstates. We use these capabilities to study Bloch oscillations, spin–momentum locking and Van Hove singularities in the transition density of states. Our results lay the groundwork for using fermionic optical lattice clocks to probe new phases of matter.

When tunnelling is allowed, SOC for fermions emerges naturally in a nuclear-spin-polarized ^{87}Sr optical lattice clock during laser interrogation of the narrow-linewidth $^1S_0(|g\rangle) - {}^3P_0(|e\rangle)$ clock transition at wavelength $\lambda_c = 698$ nm (Fig. 1a), where $|g\rangle$ and $|e\rangle$ are the ground and excited states. The lattice used to confine the atoms has a wavelength $\lambda_L = 813$ nm. At this 'magic' wavelength[13], the band structures of the two clock states are identical, with band energies $E_{n_z}(q)$ determined by the discrete band index n_z and quasi-momentum q in units of $\hbar/a$, where $a = \lambda_L/2$ is the lattice constant and $\hbar$ is the reduced Planck constant. When an atom is excited from $|g\rangle$ to $|e\rangle$ using a clock laser with Rabi frequency Ω and frequency detuning δ from the bare clock transition, energy and momentum conservation require a change in atomic momentum of $2\pi\hbar/\lambda_c$.

The resulting Hamiltonian can be diagonalized in quasi-momentum space by performing a gauge transformation $|e,q\rangle_{n_z} \rightarrow |e,q+\phi\rangle_{n_z}$, where $\phi = \pi\lambda_L/\lambda_c \approx 7\pi/6$. Figure 1b shows the transformed $|g\rangle$ and $|e\rangle$ bands for $n_z = 0$ (the ground-state band) under the rotating-wave approximation when $\delta = 0$. The transformed spin–orbit-coupled Hamiltonian is given by[12]

$$H_{SOC} = -\hbar \sum_q \boldsymbol{B}_{n_z}(q,\Omega,\delta)\cdot\boldsymbol{S} \tag{1}$$

where the components of $\boldsymbol{S}$ are the spin-1/2 angular momentum operators $\hat{S}^{X,Y,Z}$ for the two clock states. $\boldsymbol{B}_{n_z}(q,\Omega,\delta)$ is an effective, quasi-momentum-dependent magnetic field given by

$$\begin{aligned}\boldsymbol{B}_{n_z}(q,\Omega,\delta) &= \left[B^X_{n_z}(\Omega),\ 0, B^Z_{n_z}(q,\delta)\right] \\ &= \left[\Omega,\ 0, (E_{n_z}(q) - E_{n_z}(q+\phi))/\hbar + \delta\right]\end{aligned} \tag{2}$$

where in the tight-binding limit $E_0(q) = -2\hbar J\cos(q)$, and J is the tunnelling rate between nearest-neighbour lattice sites. The eigenstates of H_{SOC} are described by Bloch vectors in the $\hat{X}$–$\hat{Z}$ plane, pointing along the magnetic field $\boldsymbol{B}_{n_z}(q,\Omega,\delta)$, with their orientations specified by the chiral Bloch vector angle θ_B with respect to the $\hat{Z}$ axis[12], where

$$\theta_B = \arctan\left[\frac{\Omega}{(E_{n_z}(q) - E_{n_z}(q+\phi))/\hbar + \delta}\right] \tag{3}$$

The q dependence of θ_B is a manifestation of chiral spin–momentum locking[12,14].

To connect this system to related works on synthetic gauge fields[1,2,6–8,11,15,16], we can treat the internal clock transition ($|g\rangle \rightarrow |e\rangle$) as a synthetic dimension[17], as shown in Fig. 1a. In this case, an atom following a closed trajectory about a single plaquette ($|m,g\rangle \rightarrow |m+1,g\rangle \rightarrow |m+1,e\rangle \rightarrow |m,e\rangle \rightarrow |m,g\rangle$) accumulates a phase ϕ, which resembles the flux experienced by a charged particle in the presence of an external magnetic field. In this equally valid description, the chiral Bloch vector angle θ_B is directly connected to the topological nature of chiral edge modes of the two-dimensional Hofstadter model[8,14]. Coupling multiple nuclear spin states with our synthetic gauge fields should enable the realization of topological bands[1,2,5] and exotic phases in higher dimensions[18].

In our experiment, several thousand nuclear-spin-polarized fermionic ^{87}Sr atoms are cooled to temperatures of about 2 μK and loaded into a horizontal one-dimensional optical lattice aligned along the $\hat{z}$ axis. The lattice is formed using a high-power ($P_1 \approx 3$ W) incoming beam that is focused down to a beam waist $w_0 \approx 45$ μm and a strongly attenuated retro-reflection with tunable power ($0 \leq P_2 \leq 50$ mW; Fig. 1a). This method enables the radial trap frequency to effectively remain constant at $\nu_r \approx 450$ Hz, while the axial trapping potential U_z can be tuned via P_2 over a wide range from $U_z/E_r = 0$ to $U_z/E_r > 200$, where $E_r = \hbar^2 k_L^2/(2m)$ is the lattice recoil energy and m is the atomic mass. This range of U_z corresponds to axial trap frequencies $\nu_z \approx 2E_r\sqrt{U_z/E_r}/(2\pi\hbar)$ up to about 100 kHz. When $\nu_z \gtrsim 40$ kHz, the timescale of site-to-site tunnelling is longer than experimentally relevant timescales and so the atoms are effectively localized to single lattice sites, as is standard in optical lattice clock operation[13]. However, for smaller ν_z, tunnelling between nearest-neighbour lattice sites is important, and occurs at a rate $J_{\boldsymbol{n}_r}$ that depends on the radial mode index $\boldsymbol{n}_r$. In this regime, atomic motion in the axial direction is described by delocalized Bloch states characterized by n_z and q. For a thermal distribution of approximately 2 μK, the atoms are predominantly in the $n_z = 0$ axial ground band and completely fill the band. The average radial mode occupation $|\boldsymbol{n}_r| \approx 100$.

The clock laser is locked to an ultra-stable optical cavity[13] with a linewidth of approximately 26 mHz. Because the clock laser is collinear with the lattice axis, coupling to the radial motional modes is suppressed and we treat the system as quasi-one-dimensional, with relatively minor corrections arising from the thermal average of

[1]JILA, NIST and University of Colorado, Department of Physics, University of Colorado, Boulder, Colorado 80309, USA. †Present addresses: The Johns Hopkins Applied Physics Laboratory, Laurel, Maryland 20723, USA (M.L.W.); International Center for Quantum Materials, School of Physics, Peking University, Beijing 100871, China (X.Z.).
*These authors contributed equally to this work.

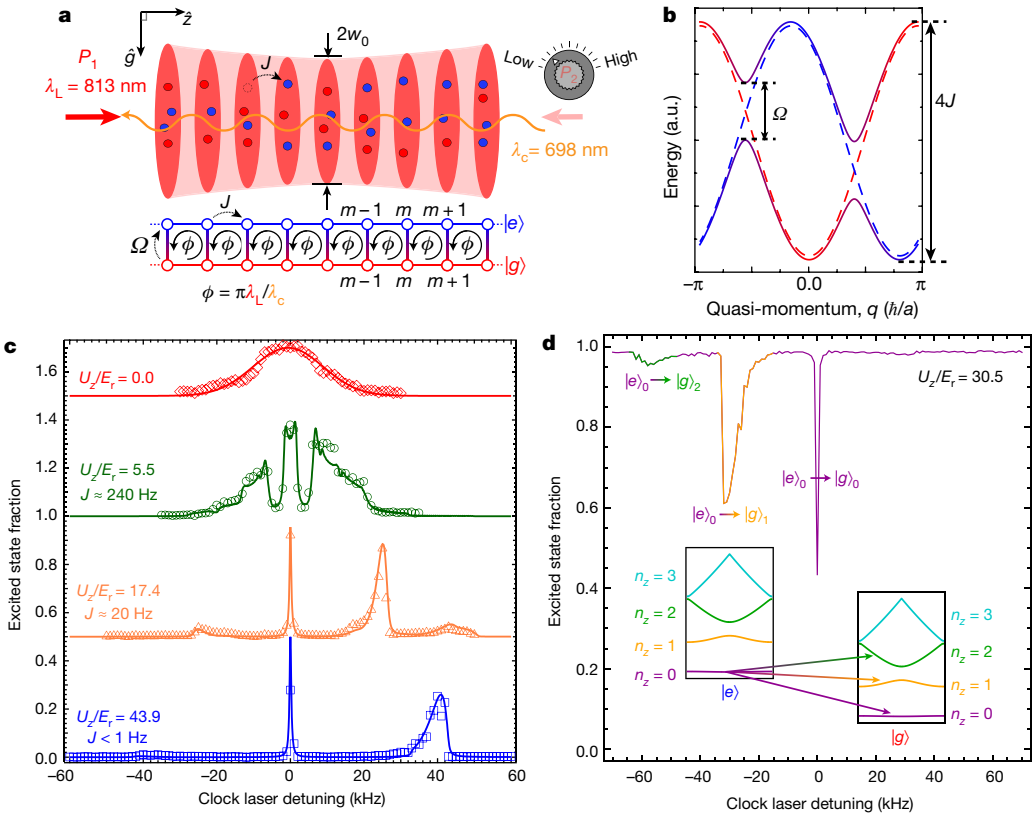

Figure 1 | Spin–orbit-coupled fermions in an optical lattice clock with tunable tunnelling. a, Top, atoms are trapped in a one-dimensional optical lattice with a beam waist w_0, formed by interfering a strong trapping beam (red arrow; power P_1, wavelength $\lambda_L = 813$ nm) with a counter-propagating, tunably attenuated retro-reflection (pink arrow; variable power P_2). The atoms, which are shown in both the ground (red) and excited (blue) clock states, are probed on the narrow clock transition with an ultra-stable clock laser (orange waveform; $\lambda_c = 698$ nm, Rabi frequency Ω). The atoms tunnel to neighbouring lattice sites at a rate J, which can be tuned by varying P_2. The axis $\hat{z}$ of the one-dimensional lattice is horizontal with respect to the axis of gravity $\hat{g}$. Bottom, the resulting spin–orbit-coupled Hamiltonian is equivalent to that of charged fermions on a synthetic two-dimensional ladder with horizontal tunnelling rate J between neighbouring physical lattice sites m, $m+1$, …, vertical tunnelling rate Ω between the ground and excited clocks states $|g\rangle$ and $|e\rangle$, and a synthetic magnetic field flux $\phi = \pi\lambda_L/\lambda_c$. **b**, The clock laser couples the dispersion curve for $|g\rangle_0$ (dashed red line) to the quasi-momentum-shifted curve for $|e\rangle_0$ (dashed blue line), resulting in spin–orbit-coupled bands (solid dichromatic lines), with the splitting between the bands given by Ω, and the bandwidth of each of the uncoupled bands given by $4J$. The y-axis is energy in arbitrary units (a.u.). **c**, Clock spectroscopy ($\Omega \approx 2\pi \times 200$ Hz, 80-ms pulse duration) at four axial trapping potentials (U_z/E_r; data and fits are vertically separated for clarity). When $P_2 = 0$, the sidebands and carrier merge into a Doppler-broadened Gaussian (red diamonds). The solids lines represent theoretical calculations using a model that treats the axial and radial coupling perturbatively (see Methods). **d**, Spectroscopy of atoms in $|e\rangle_0$, prepared by driving the $|g\rangle_0 \rightarrow |e\rangle_0$ transition and then removing any remaining atoms in $|g\rangle$. Inset, the Bloch bands for the $|g\rangle$ and $|e\rangle$ clock states, and the inter-band and carrier transitions out of $|e\rangle_0$. The colours of the final bands correspond to the colours of the respective transition peaks in the main panel. In **c** and **d**, each data point corresponds to a single measurement sequence with a new sample of thousands of ^{87}Sr atoms.

the Rabi frequency Ω_{n_r} and the tunnelling rate J_{n_r} over the radial mode occupation. Therefore, for the sake of clarity, we drop the radial mode index from Ω and J. The clock laser Rabi frequency Ω is measured on resonance with the carrier at $\delta = 0$ with a high axial trapping frequency $\nu_z > 50$ kHz. The mean particle number per lattice site was kept in the range $N \approx 1$–10, which for the operating conditions used results in a density-dependent many-body interaction rate of $N\chi/(2\pi) \lesssim 1$ Hz, where χ is the two-body interaction rate[19]. For the experiments presented here, $\Omega \gg N\chi$ and so the results are well described by a single-particle model.

Unlike previous studies of SOC in ultracold atoms, for which time-of-flight imaging was used to determine the momentum distribution[1–11], all of the data presented here is measured *in situ* using clock spectroscopy[13]. Clock spectroscopy provides precise measurement and control of the atomic spin and motional degrees of freedom and access to the atomic density of states, and offers the prospect for real-time, non-destructive measurement of atom dynamics in the lattice. At the end of each experiment, the number of atoms in each of the $|e\rangle$ and $|g\rangle$ states is counted using a cycling transition (see Methods) and the normalized population fraction in each state is extracted. For example, Fig. 1c presents spectroscopy of the carrier and motional sideband transitions at four different axial trapping potentials, with the atoms initially prepared in the ground clock state and ground Bloch band, $|g\rangle_0$. At $U_z/E_r = 43.9$ (blue squares in Fig. 1c) the atoms are strongly confined and the data are well described by a model that neglects tunnelling between lattice sites[20]. However, as P_2 is turned down and the trapping potential is reduced to $U_z/E_r = 5.5$ (green circles), the carrier transition exhibits a broad splitting of two sharp resonances, which is inconsistent with atoms localized to single sites. A model that treats the axial and radial coupling perturbatively[20] fully reproduces the measured line shapes (solid lines in Fig. 1c; see Methods).

The narrow $|g\rangle_0 \rightarrow |e\rangle_0$ carrier transition centred at $\delta/(2\pi) = 0$ kHz enables the preparation of atoms in the excited clock state and ground Bloch band $|e\rangle_0$, from which spectroscopy can also be performed, as shown in Fig. 1d. Owing to the long lifetime of $|e\rangle$, we do not observe spin state relaxation to $|g\rangle$ over the timescales explored in this experiment (<150 ms; see Methods). In addition to the carrier transition, motional sidebands corresponding to axial inter-band transitions are also apparent in Fig. 1c. The measured line shape in this case is also

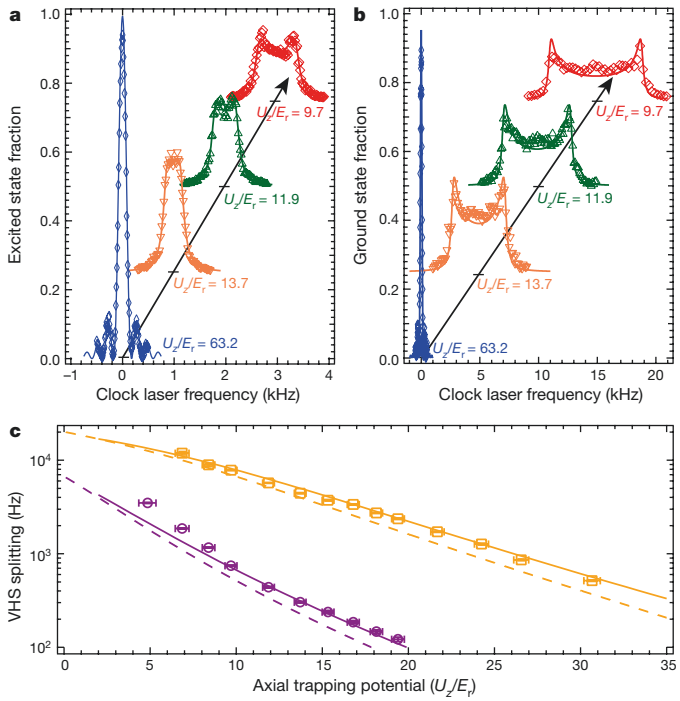

Figure 2 | Van Hove singularities and band mapping. a, Excited state fraction following a π pulse ($\Omega = 2\pi \times 100$ Hz) at four axial trapping potentials U_z/E_r, with the atoms initially prepared in $|g\rangle_0$. The split peaks for $U_z/E_r \leq 13.7$ are a result of divergences in the atomic density of states known as Van Hove singularities (VHSs). The fits are a convolution of the expected joint transition density of states for the spin–orbit-coupled bands with the measured Rabi line shape at high U_z/E_r (see Methods). **b**, Ground state fraction following a Rabi pulse for the same potentials as in **a**, with the atoms initially prepared in $|e\rangle_1$. The duration of the Rabi pulse was varied to improve population contrast (see Methods). In **a** and **b**, each data point corresponds to a single measurement sequence with a new sample of thousands of ^{87}Sr atoms. The data and fits are offset vertically and horizontally for clarity. The diagonal axes are included as guides to the eye, with the tick marks corresponding to zero detuning and zero excited or ground state fraction for each measured line shape. **c**, The splitting between the VHS peaks in the $|g\rangle_0 \rightarrow |e\rangle_0$ (purple circles) and $|e\rangle_1 \rightarrow |g\rangle_1$ (orange squares) transitions as a function of trapping potential, extracted using fits as shown in **a** and **b**. Horizontal error bars are 1σ standard error estimates from spectroscopy of the axial sidebands; vertical error bars are 1σ standard error estimates for the extracted VHS splitting. The no-free-parameter VHS splittings predicted for atoms in the ground and first-excited bands of a one-dimensional sinusoidal lattice (purple and orange dashed lines, respectively) and the splittings predicted by a model that includes the transverse motional modes and finite atomic temperatures (solid lines) are shown for comparison.

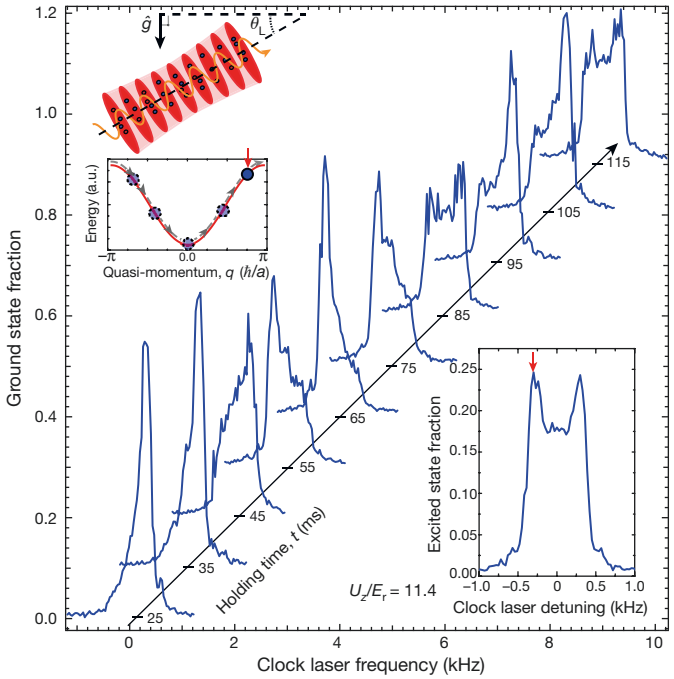

Figure 3 | Bloch oscillations. Lower-right inset, the split Rabi lines shown in Fig. 2a, b enable the spectral selection of atoms with a particular quasi-momentum q^*. At a trapping potential of $U_z/E_r = 11.4$, a π pulse ($\Omega = 2\pi \times 100$ Hz) tuned to the left VHS peak is applied (red arrow) and the remaining ground state atoms are removed. Upper-left inset, the lattice is tilted by an angle $\pi/2 - \theta_L$ with respect to gravity $\hat{g}$ (top). As a result, the atoms initially prepared with $q^* \approx \pi$ (red arrow) undergo Bloch oscillations, with their quasi-momenta cycling through the entire band (bottom). Main panel, following a variable wait time t from the end of the first π pulse, a second π pulse is applied, revealing a highly asymmetric line shape (first blue curve at 25 ms). The atoms undergo Bloch oscillations, resulting in periodic oscillations of the line shape as the waiting time between the first and second pulse is varied. The curves are horizontally and vertically offset as a function of wait time for clarity. Each data point corresponds to a single measurement sequence with a new sample of thousands of ^{87}Sr atoms.

fully captured by the perturbative model (solid lines; see Methods). At high trapping potential (blue squares in Fig. 1c), the prominent blue-detuned sideband at $\delta/(2\pi) \approx 40$ kHz corresponds to the $|g\rangle_0 \rightarrow |e\rangle_1$ transition, where $|e\rangle_1$ refers to the atoms in the excited clock state and first excited Bloch band. The corresponding red-detuned sideband at $\delta/(2\pi) \approx -40$ kHz is suppressed because the atoms have been prepared predominantly in the $n_z = 0$ ground band. The inter-band transitions can also be used to selectively prepare the atoms in specific Bloch bands. For example, to prepare atoms exclusively in the $n_z = 1$ band, a clock laser pulse is applied to the $|g\rangle_0 \rightarrow |e\rangle_1$ blue sideband transition. A strong 'clearing' pulse is then applied to remove any remaining atoms in $|g\rangle$, leaving atoms in $|e\rangle$ unperturbed. The remaining atoms are thus purified in the $n_z = 1$ Bloch band and can be used for further experiments or measurements.

In Fig. 2, we demonstrate the use of selective band preparation to probe the effect of SOC on the $|g\rangle_0 \rightarrow |e\rangle_0$ and $|e\rangle_1 \rightarrow |g\rangle_1$ carrier transitions. In Fig. 2a, the atoms are initially prepared in $|g\rangle_0$ and a π pulse of the clock laser is applied. At $U_z/E_r = 63.2$ (narrow blue diamonds) the $|g\rangle_0 \rightarrow |e\rangle_0$ transition has a typical Fourier-limited Rabi line shape. However, as U_z is reduced (but in the regime $U_z > E_r$), the transition begins to broaden and splits into two peaks, with the splitting scaling proportionally to the tunnelling rate in the lowest Bloch band, which scales[3] as

$$J \approx \frac{4}{\hbar\sqrt{\pi}} E_r \left(\frac{U_z}{E_r}\right)^{3/4} \exp\left(-2\sqrt{\frac{U_z}{E_r}}\right)$$

As shown in Fig. 2b, the same behaviour is observed when the atoms are initially prepared in the $|e\rangle_1$ state, with the $|e\rangle_1 \rightarrow |g\rangle_1$ transition exhibiting much larger splitting compared to the $|g\rangle_0 \rightarrow |e\rangle_0$ transition for the same axial potential.

The split line shapes of the clock carrier transition at low U_z, which have been theoretically predicted[12,21], can be understood by considering the band dispersion curves presented in Fig. 1b. Because the quasi-momentum dependence of the $|g\rangle_0$ and $|e\rangle_0$ bands differ by ϕ (see equations (1) and (2)), the transition frequency is q dependent. In the tight-binding approximation, the largest momentum-induced detuning from the bare clock transition frequency is given by $\Delta = 4J|\sin(\phi/2)|$, where $4J$ is the bandwidth of the $n_z = 0$ ground band and $\sin(\phi/2) = 0.97 \approx 1$, which results in an overall broadening of the transition by $2\Delta \approx 8J$. The probability of a transition between the two bands at a specific q is then determined by the joint transition density of states, which diverges at saddle points in the energy difference

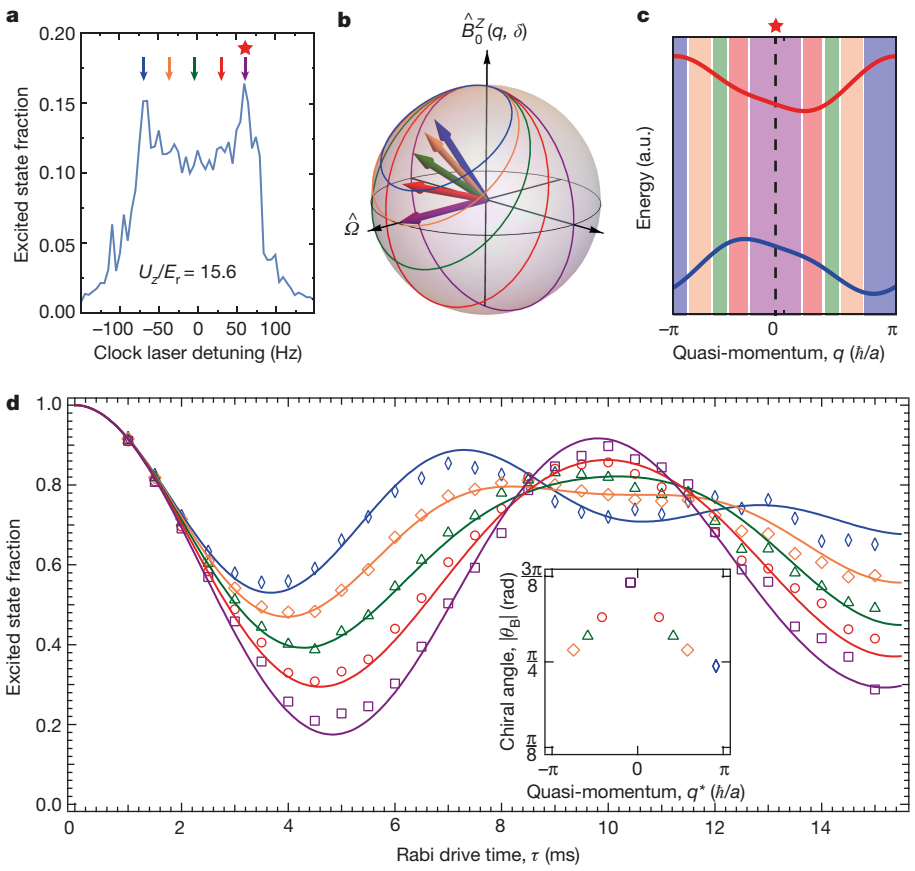

Figure 4 | Rabi measurements of the chiral Bloch vector. a, Atoms are selectively prepared in a quasi-momentum window using a π pulse ($\Omega = 2\pi \times 10$ Hz,) with five different pulse detunings (coloured arrows). An axial potential of $U_z/E_r = 15.6$ is used, resulting in $\Delta/(2\pi) \approx 67$ Hz. A second, stronger Rabi pulse ($\Omega = 2\pi \times 100$ Hz) tuned to the right VHS peak (red star) is used to generate SOC. **b**, The chiral Bloch vectors corresponding to the detunings in **a** are shown as arrows, along with the clock state spin precession for each vector (corresponding coloured lines) where $\hat{\Omega}$ and $\hat{B}_0^Z(q, \delta)$ are the axes of the Bloch sphere as defined in the spin–orbit-coupled Hamiltonian (equations (1) and (2)). **c**, The spin–orbit-coupled band structure experienced by the atoms during the second pulse, with each quasi-momentum window colour-coded to match the detunings in **a**. The clock states are completely mixed by SOC at $q = 0$. At quasi-momenta far from $q = 0$, the red band has more of the character of $|g\rangle$, while the blue band has more of the character of $|e\rangle$. The selection windows overlap; the width of each window is for illustrative purposes only, to indicate the relative values. **d**, Excited state fraction as a function of the duration of the second pulse τ for the five initial pulse detunings shown in **a** (colour-coded data points), along with the no-free-parameter dynamics predicted by a semi-classical model (solid lines; see Methods). Inset, corresponding chiral Bloch vector angle θ_B extracted for each quasi-momentum window centred at q^*. In **a** and **d**, each data point corresponds to a single measurement sequence with a new sample of thousands of ^{87}Sr atoms.

between the band dispersion curves. These divergence points in the density of states of a crystalline lattice are called Van Hove singularities (VHSs) and are well known from optical absorption spectra in solids and scanning tunnelling microscopy[22,23]. The measured line shapes are a convolution of the atomic transition density of states with the Rabi line shape for a single atom (see Methods). For $\Delta > \Omega$ two VHS peaks (at $\delta = \pm\Delta$) are evident; at higher trapping potentials, $\Delta \ll \Omega$ and the two VHS peaks merge to give the standard Rabi line shape (Fig. 2a, b).

Optical clock spectroscopy also provides a direct, *in situ* probe of the Bloch bandwidths, and thus of the tunnelling rate J, through the VHS splitting. We demonstrate this technique by measuring Rabi line shapes at a range of axial potentials from $U_z/E_r = 5.5$ to $U_z/E_r = 63.2$ and then fitting a convolution of the joint transition density of states for the spin–orbit-coupled bands with the measured Rabi line shape at high U_z/E_r to extract the VHS splitting (example fits are shown in Fig. 2a, b; see Methods). The extracted splittings for the $|g\rangle_0 \rightarrow |e\rangle_0$ (purple circles) and $|e\rangle_1 \rightarrow |g\rangle_1$ (orange squares) transitions are plotted as a function of trapping potential in Fig. 2c. Only splittings for which the two peaks are resolvable are shown. At $U_z/E_r = 5.5$ the VHS splitting of the $|e\rangle_1 \rightarrow |g\rangle_1$ transition overlapped with the inter-band transitions and the splitting could not be unambiguously extracted. The no-free-parameter VHS splitting that is anticipated for spin–orbit-coupled fermions in a one-dimensional lattice (purple and orange dashed lines for $n_z = 0$ and $n_z = 1$, respectively, in Fig. 2c) and the splitting that is predicted by the perturbative model (solid lines) are shown for comparison. The origin of the slight difference between the experimental data and the model prediction in the ground band at lower trapping potentials might be related to inhomogeneities in the axial trapping potential across the populated lattice sites or to an incomplete theoretical description of the coupling between the axial and radial modes.

Just as the spectroscopically resolved sidebands enabled band preparation, the quasi-momentum dependence of the clock transition frequency enables the selective preparation and subsequent manipulation of atoms with particular quasi-momenta (Fig. 3). Following initialization in the $|g\rangle_0$ state, a clock pulse with Rabi frequency $\Omega < 2\Delta$ is applied to the carrier transition with a detuning $|\delta^*| \leq \Delta$. Only atoms with quasi-momenta in a window centred around $q^* \approx \arccos(\delta^*/\Delta)$ and with a width bounded by $2\pi\Omega/\Delta$ will be excited to $|e\rangle_0$; atoms with quasi-momenta outside this window will be left in $|g\rangle$. A strong clearing pulse is applied to remove atoms in $|g\rangle$, leaving only the atoms in $|e\rangle_0$ with quasi-momenta in the window centred around q^*. Following a variable wait time t, a second π pulse is used to measure the line shape. If the lattice is tilted with respect to gravity, then the atoms will undergo Bloch oscillations during the wait time[24], with their quasi-momenta evolving as $q(t) = q_0 + \nu_B t$, where q_0 is the initial quasi-momentum of the atom and the value of $q(t)$ is restricted to the first Brillouin zone, and the Bloch oscillation frequency $\nu_B = mg\lambda_L \sin(\theta_L)/(4\pi\hbar)$, where g is the acceleration due to gravity and θ_L is the angle of tilt of the lattice. In this *in situ* observation of Bloch oscillations in a tilted lattice[25], the highly asymmetric line shapes oscillate back and forth as the quasi-momenta cycle through the Brillouin zone at a frequency of $\nu_B = 14$ Hz, which corresponds to a lattice tilt of $\theta_L = 16 \times 10^{-3}$ rad.

We characterize the q dependence of the chiral Bloch vector angle θ_B (equation (3)) using the same quasi-momentum selection technique that was used to observe Bloch oscillations. For these measurements the lattice tilt was adjusted to minimize $\nu_B \leq 3$ Hz, with $\theta_L \leq 3.5 \times 10^{-3}$ rad. As shown in Fig. 4a, atoms are prepared in $|e\rangle_0$ with quasi-momentum q^*. In five separate experiments, q^* is varied using a range of detunings δ^* spanning the two VHS peaks (coloured arrows). A strong Rabi pulse of duration τ is applied with detuning δ corresponding to the right VHS peak (red star in Fig. 4a), generating SOC with the corresponding q^*-dependent chiral Bloch vector (pointing along the direction of the effective magnetic field $\boldsymbol{B}_{n_z}(\Omega, q, \delta)$, equation (2)) shown in Fig. 4b, and with the SOC band structure shown in Fig. 4c. In Fig. 4d, the resultant population fraction in $|e\rangle$ for each prepared q^* is plotted as a function of the evolution time τ. The dynamics are entirely captured by the q^*-dependent spin precessions

about the chiral Bloch vectors (eigenstates of equation (1)), depicted in Fig. 4b. The theoretical calculations involve no free parameters and use only the experimental values of δ^*, δ, ν_B and Ω (solid lines in Fig. 4d; see Methods). The dephasing of the spin precession at longer τ is well described by the known initial distribution of quasi-momenta q^* (see Methods), and could be mitigated by reducing the Rabi frequency used for the q^* selection with respect to the VHS splitting 2Δ, at the cost of reduced signal-to-noise ratio due to the smaller number of atoms selected. In the inset of Fig. 4d we plot the corresponding chiral Bloch vector angle $|\theta_B|$ that was extracted for each initial pulse detuning as a function of prepared quasi-momentum q^*. Because there is a one-to-one correspondence between the topological chiral edge modes of the two-dimensional Hofstadter model[15,16] and the energy bands and eigenstates of the synthetic ladder[8,14] shown in Fig. 1a, the q^* dependence of $|\theta_B|$ that we measure spectroscopically is a direct manifestation of the well-defined chirality of the edge states of the Hofstadter Hamiltonian. The presence of spin–momentum locking in the eigenmodes of the ladder has previously been observed using time-of-flight imaging[6–8].

We have studied spin–orbit-coupled fermions in an optical lattice clock and characterized the associated synthetic momentum-dependent magnetic field. We observed clean experimental signatures of SOC physics at microkelvin temperatures without cooling to Fermi degeneracy, and observed no decoherence or heating on timescales of hundreds of milliseconds. The recent realization of a Fermi-degenerate three-dimensional optical lattice clock (S. L. Campbell *et al.*, manuscript in preparation) opens the possibility of implementing two- and three-dimensional SOC, tuning the SOC phase ϕ and reaching the lower temperatures that are required for the preparation of new many-body states[1,2,4,5,26]. Although we have focused entirely on single-particle physics, many-body correlations and SU(N) symmetry have previously been observed in optical lattice clocks[19,27], offering prospects for studying the interplay between SOC and interactions in higher synthetic dimensions[1,2,4,5,17,18].

Following the completion of this work, implementations of SOC using the direct optical transition in ^{173}Yb atoms[28] and using a two-dimensional manifold of discrete atomic momentum states in ^{87}Rb atoms[29] were reported.

Online Content Methods, along with any additional Extended Data display items and Source Data, are available in the online version of the paper; references unique to these sections appear only in the online paper.

Received 10 August; accepted 8 November 2016.
Published online 21 December 2016.

1. Dalibard, J., Gerbier, F., Juzeliūnas, G. & Öhberg, P. *Colloquium*: Artificial gauge potentials for neutral atoms. *Rev. Mod. Phys.* **83,** 1523–1543 (2011).
2. Goldman, N., Juzeliūnas, G., Öhberg, P. & Spielman, I. Light-induced gauge fields for ultracold atoms. *Rep. Prog. Phys.* **77,** 126401 (2014).
3. Bloch, I., Dalibard, J. & Zwerger, W. Many-body physics with ultracold gases. *Rev. Mod. Phys.* **80,** 885–964 (2008).
4. Galitski, V. & Spielman, I. B. Spin–orbit coupling in quantum gases. *Nature* **494,** 49–54 (2013).
5. Zhai, H. Degenerate quantum gases with spin–orbit coupling: a review. *Rep. Prog. Phys.* **78,** 026001 (2015).
6. Stuhl, B., Lu, H.-I., Aycock, L., Genkina, D. & Spielman, I. Visualizing edge states with an atomic Bose gas in the quantum Hall regime. *Science* **349,** 1514–1518 (2015).
7. Mancini, M. *et al.* Observation of chiral edge states with neutral fermions in synthetic Hall ribbons. *Science* **349,** 1510–1513 (2015).
8. Atala, M. *et al.* Observation of chiral currents with ultracold atoms in bosonic ladders. *Nat. Phys.* **10,** 588–593 (2014).
9. Burdick, N. Q., Tang, Y. & Lev, B. L. Long-lived spin–orbit-coupled degenerate dipolar Fermi gas. *Phys. Rev. X* **6,** 031022 (2016).
10. Song, B. *et al.* Spin–orbit coupled two-electron Fermi gases of ytterbium atoms. Preprint at https://arxiv.org/abs/1608.00478 (2016).
11. Li, J. *et al.* Spin–orbit coupling and spin textures in optical superlattices. *Phys. Rev. Lett.* **117,** 185301 (2016).
12. Wall, M. L. *et al.* Synthetic spin–orbit coupling in an optical lattice clock. *Phys. Rev. Lett.* **116,** 035301 (2016).
13. Bloom, B. J. *et al.* An optical lattice clock with accuracy and stability at the 10^{-18} level. *Nature* **506,** 71–75 (2014).
14. Hügel, D. & Paredes, B. Chiral ladders and the edges of quantum Hall insulators. *Phys. Rev. A* **89,** 023619 (2014).
15. Aidelsburger, M. *et al.* Realization of the Hofstadter Hamiltonian with ultracold atoms in optical lattices. *Phys. Rev. Lett.* **111,** 185301 (2013).
16. Miyake, H., Siviloglou, G. A., Kennedy, C. J., Burton, W. C. & Ketterle, W. Realizing the Harper Hamiltonian with laser-assisted tunneling in optical lattices. *Phys. Rev. Lett.* **111,** 185302 (2013).
17. Celi, A. *et al.* Synthetic gauge fields in synthetic dimensions. *Phys. Rev. Lett.* **112,** 043001 (2014).
18. Barbarino, S., Taddia, L., Rossini, D., Mazza, L. & Fazio, R. Magnetic crystals and helical liquids in alkaline-earth fermionic gases. *Nat. Commun.* **6,** 8134 (2015).
19. Martin, M. J. *et al.* A quantum many-body spin system in an optical lattice clock. *Science* **341,** 632–636 (2013).
20. Blatt, S. *et al.* Rabi spectroscopy and excitation inhomogeneity in a one-dimensional optical lattice clock. *Phys. Rev. A* **80,** 052703 (2009).
21. Lemonde, P. & Wolf, P. Optical lattice clock with atoms confined in a shallow trap. *Phys. Rev. A* **72,** 033409 (2005).
22. Van Hove, L. The occurrence of singularities in the elastic frequency distribution of a crystal. *Phys. Rev.* **89,** 1189–1193 (1953).
23. Kim, P., Odom, T. W., Huang, J.-L. & Lieber, C. M. Electronic density of states of atomically resolved single-walled carbon nanotubes: Van Hove singularities and end states. *Phys. Rev. Lett.* **82,** 1225–1228 (1999).
24. Ben Dahan, M., Peik, E., Reichel, J., Castin, Y. & Salomon, C. Bloch oscillations of atoms in an optical potential. *Phys. Rev. Lett.* **76,** 4508–4511 (1996).
25. Preiss, P. M. *et al.* Strongly correlated quantum walks in optical lattices. *Science* **347,** 1229–1233 (2015).
26. Isaev, L., Schachenmayer, J. & Rey, A. Spin–orbit-coupled correlated metal phase in Kondo lattices: an implementation with alkaline-earth atoms. *Phys. Rev. Lett.* **117,** 135302 (2016).
27. Zhang, X. *et al.* Spectroscopic observation of SU(N)-symmetric interactions in Sr orbital magnetism. *Science* **345,** 1467–1473 (2014).
28. Livi, L. F. *et al.* Synthetic dimensions and spin–orbit coupling with an optical clock transition. *Phys. Rev. Lett.* **117,** 220401 (2016).
29. An, F. A., Meier, E. J. & Gadway, B. Direct observation of chiral currents and magnetic reflection in atomic flux lattices. Preprint at https://arxiv.org/abs/1609.09467 (2016).

Acknowledgements We are grateful to N. R. Cooper for insights and discussions, and S. L. Campbell, N. Darkwah Oppong, A. Goban, R. B. Hutson, D. X. Reed, J. Robinson, L. Sonderhouse and W. Zhang for technical contributions and discussions. This research is supported by NIST, the NSF Physics Frontier Center at JILA (NSF-PFC-1125844), AFOSR-MURI, AFOSR, DARPA and ARO. S.K., M.L.W. and G.E.M. acknowledge the NRC postdoctoral fellowship programme.

Author Contributions S.K., S.L.B., T.B., G.E.M., X.Z. and J.Y. contributed to the experiments. M.L.W., A.P.K. and A.M.R. contributed to the development of the theoretical model. All authors discussed the results, contributed to the data analysis and worked together on the manuscript.

Author Information Reprints and permissions information is available at www.nature.com/reprints. The authors declare no competing financial interests. Readers are welcome to comment on the online version of the paper. Correspondence and requests for materials should be addressed to S.K. (shimonk@jila.colorado.edu).

Reviewer Information *Nature* thanks L. Duan and the other anonymous reviewer(s) for their contribution to the peer review of this work.

METHODS

Experimental methods. *Measurement protocol.* To load the optical lattice, ^{87}Sr atoms are cooled with two sequential three-dimensional magneto-optical traps—the first using the strong $^1S_0 \rightarrow {}^1P_1$ transition (461 nm) and the second using the narrower $^1S_0 \rightarrow {}^3P_1$ transition (689 nm). Following the second magneto-optical trap, the atoms are sufficiently cold and dense to be trapped in the optical lattice. Once in the lattice, the atoms are first nuclear spin-polarized and then further cooled using axial sideband and radial Doppler cooling on the 689-nm transition.

At the end of each experiment, the population of the $|g\rangle$ state is measured by driving the atoms on the 461-nm cycling transition and counting the emitted photons. After 5 ms, all $|g\rangle$ atoms have been heated out of the lattice, at which point the atoms in $|e\rangle$ are optically pumped into the $|g\rangle$ state and are counted in the same manner. A 5-ms-long 461-nm pulse is also used as the 'clearing' pulse to remove ground state atoms in the protocols used for preparing atoms in specific bands and with select quasi-momenta.

Characterization of the trapping potential. The cylindrically symmetric trapping potential experienced by an atom at position z along the axis of propagation of the lattice beams and a distance r from the centre of the beams is given by

$$V(r,z) = -[V_{\mathrm{const}} + U_z \cos^2(k_{\mathrm{L}} z)]\mathrm{e}^{-2r^2/w_0^2} \tag{4}$$

where

$$V_{\mathrm{const}} = \alpha(\lambda_{\mathrm{L}})\frac{P_1 + P_2 - 2\sqrt{P_1 P_2}}{\pi\varepsilon_0 c w_0^2}$$

$$U_z = 4\alpha(\lambda_{\mathrm{L}})\frac{\sqrt{P_1 P_2}}{\pi\varepsilon_0 c w_0^2}$$

$k_{\mathrm{L}} = 2\pi/\lambda_{\mathrm{L}}$, ε_0 is the permittivity of free space, c is the speed of light and $\alpha(\lambda_{\mathrm{L}})$ is the a.c. polarizability evaluated at λ_{L}. Because $P_1 \gg P_2$, to first order the trapping potential in the radial direction V_{const} is proportional to P_1 and the periodic axial trapping potential U_z is proportional to $\sqrt{P_1 P_2}$. In contrast to previous experiments that generate synthetic gauge fields by periodically shaking the optical lattice potential[30–33], here the lattice potential is kept constant, and it is the probing laser itself that induces the SOC.

Band preparation. In Extended Data Fig. 1, we demonstrate the way in which the inter-band transitions can be used for band preparation. Extended Data Fig. 1a shows spectroscopy of the carrier and inter-band transitions from the initial $|g\rangle_0$ state. To prepare atoms exclusively in the $n_z = 1$ band, a clock laser pulse is applied to the $|g\rangle_0 \rightarrow |e\rangle_1$ blue sideband transition, which is at a detuning of $\delta/(2\pi) \approx \nu_z - E_{\mathrm{r}}/(2\pi\hbar) = 35$ kHz for $U_z/E_{\mathrm{r}} = 30.5$. A strong clearing pulse is then applied to remove any remaining atoms in $|g\rangle$, leaving atoms in $|e\rangle$ unperturbed. The remaining atoms are thus purified in the $n_z = 1$ Bloch band and can be used for further experiments or measurements. Extended Data Fig. 1b shows spectroscopy of the sidebands following this protocol, with the anharmonicity of the band spacing resulting in an unequal frequency spacing between the $|e\rangle_1 \rightarrow |g\rangle_2$ and $|e\rangle_1 \rightarrow |g\rangle_0$ sideband transitions about the $|e\rangle_1 \rightarrow |g\rangle_1$ carrier transition. The transitions out of $|e\rangle_0$ from Fig. 1d are shown for comparison. In contrast to previous experiments[34,35], no band relaxation was observed out of the $|e\rangle_1$ state over a waiting time of greater than 500 ms, owing to the dilute atomic conditions achieved in our experiment.

Measurements of axial heating and loss rates. The axial heating rate in our lattice was measured using spectroscopy of the axial motional sidebands. The atoms were prepared in $|e\rangle_0$, and the clock laser was applied on resonance with the carrier transition for a variable wait time of up to 155 ms. The atoms in $|g\rangle$ were removed with a clearing pulse and spectroscopy of the remaining atoms in $|e\rangle$ was performed. The axial sideband asymmetry was then used to determine the temperature and heating rate. The measurement was performed in both the strong confinement ($U_z/E_{\mathrm{r}} \approx 200$) and tunnelling-allowed ($U_z/E_{\mathrm{r}} \approx 10$) regimes. In both cases, the results were consistent with no axial heating over the 155-ms wait time. This is consistent with previous measurements of the temperature dependence of the clock transition coherence[20].

The loss rates out of $|e\rangle$ were measured by preparing the atoms in $|e\rangle_0$, leaving the atoms in the dark for a variable wait time of up to 1.5 s and then counting the number of atoms in the $|e\rangle$ and $|g\rangle$ states. Loss of atoms due to inelastic p-wave e–e scattering was observed with a density-dependent loss rate consistent with previous measurements[36]. For the atomic densities used here, the measured loss rate corresponded to approximately 1.5 s^{-1} and so did not have an impact on the measurements presented, owing to their shorter timescales. For future many-body experiments with higher desired densities, the temperature can be lowered by loading the lattice from a Fermi-degenerate gas (S. L. Campbell *et al.*, manuscript in preparation), in which case the inelastic p-wave e–e collisions will be greatly suppressed. An additional one-body loss rate of approximately 0.2 s^{-1} was observed, consistent with the vacuum-limited lifetime in the chamber. Finally, a $|e\rangle \rightarrow |g\rangle$ spin-flip rate of about 0.1 s^{-1} was observed, consistent with previously measured two-photon Raman scattering from the lattice light via the $^3P_1$ state[37]. Although this spin-flip rate is negligible for the measurements presented here, it may set a limit on future SOC experiments, potentially requiring a different lattice geometry.

Theoretical methods. *Perturbative model.* For the experimental temperatures and loading conditions we used, to an excellent approximation we can treat the coupling between the axial and radial degrees of freedom perturbatively and expand equation (4) up to second order in r:

$$V(r,z) = V_z(z) + V_r(r) + \eta V_{\mathrm{coupl}}(r,z) + \mathcal{O}(r^4)$$

with $V_z(z) = -U_z\cos^2(k_{\mathrm{L}}z)$, $V_r(r) = m\omega_r^2 r^2/2$ and $V_{\mathrm{coupl}}(r,z) = -V_r(r)\sin^2(k_{\mathrm{L}}z)$. Here, $\omega_r = 2\sqrt{(U_z + V_{\mathrm{const}})/(mw_0^2)}$, m is the atom mass and $\eta = U_z/(U_z + V_{\mathrm{const}})$ is an expansion parameter. To zeroth order in η, the Hamiltonian is separable in r and z coordinates. In this limit, the radial eigenfunctions are harmonic oscillator functions $\langle \boldsymbol{r}|n_r, \upsilon\rangle = \phi_{n_r,\upsilon}(\boldsymbol{r})$ with eigenenergies $E_{n_r,\upsilon} = \hbar\omega_r(|\upsilon| + 2n_r + 1)$ parameterized by the radial quantum number $n_r = 0, 1, \ldots$ and the azimuthal quantum number $-n_r \le \upsilon \le n_r$. The axial eigenfunctions are Bloch functions $\langle z|n_z, q\rangle = \psi_{n_z,q}(z)$ with a band structure $E_{n_z}(q)$. For the cosinusoidal potential in consideration, the Bloch functions and band structure can be obtained analytically in terms of even and odd Mathieu functions

$$\psi_{n_z,q}(z) = \mathrm{MathieuC}\left[a(q, U_z/(4E_{\mathrm{r}})), U_z/(4E_{\mathrm{r}}), z\right] + i\,\mathrm{MathieuS}\left[a(q, U_z/(4E_{\mathrm{r}})), U_z/(4E_{\mathrm{r}}), z\right]$$

and

$$E_{n_z}(q)/E_{\mathrm{r}} = a(q, U_z/(4E_{\mathrm{r}}))$$

where the parameter a is the characteristic Mathieu value, for suitably chosen n_z-dependent ranges of q.

Treating $V_{\mathrm{coupl}}(r,z)$ using first-order perturbation theory in η yields the energies

$$E_{n_z,n_r,\upsilon}(q) = E_{n_r,\upsilon} + E_{n_z}(q) - \frac{1}{2}\eta E_{n_r,\upsilon}\langle n_z, q|\sin^2(k_{\mathrm{L}}z)|n_z, q\rangle$$

This expression generalizes that obtained in ref. 20 in the deep lattice limit to include quasi-momentum dependence of the energies and beyond-lowest-order anharmonic effects in the axial dimension. We can also analytically compute the first-order corrections in terms of the unperturbed band energies using the Feynman–Hellman theorem:

$$\langle n_z, q|\sin^2(k_{\mathrm{L}}z)|n_z, q\rangle = \left(\frac{1}{2} + \frac{\partial E_{n_z}(q)}{\partial U_z}\right)$$

This term has both q-independent and q-dependent components. The former lead to thermally dependent shifts in the mean band energies and the latter give a renormalization of the tunnelling rate, which depends on the radial temperature. We explicitly checked the validity of the perturbative energy expression by numerically finding the exact eigenstates of equation (4)[38].

Line shapes. To evaluate the line shapes we perform a thermal average using Boltzmann distributions with radial and axial temperatures T_r and T_z, respectively. The contribution to the line shape from the ℓth axial sideband, assuming atoms are initially populating the ℓ_0 band and internal state $\alpha = \pm$ (here $+$ is for g and $-$ is for e), is

$$P_\ell^{\pm} = \sum_{n_z,n_r,\upsilon,q} \frac{q_z(\ell_0, n_z, q)q_r(\ell_0, n_z, n_r, \upsilon)}{Z}\left|\frac{\Omega_{n_z',\ell,q}}{\Omega^{\pm\mathrm{eff}}_{n_z',\ell,q,n_r,\upsilon}}\right|^2 \sin^2\left[\frac{t}{2}\Omega^{\pm\mathrm{eff}}_{n_z',\ell,q,n_r,\upsilon}\right] \tag{5}$$

where $n_z' = n_z + \ell_0$ and

$$\Omega^{\pm\mathrm{eff}}_{n_z,\ell,q,n_r,\upsilon} \equiv \sqrt{|\Omega_{n_z,\ell,q}|^2 + [\pm\delta - [E_{n_z+\ell,n_r,\upsilon}(q+\phi) - E_{n_z,n_r,\upsilon}(q)]/\hbar]^2}$$

is the effective Rabi frequency,

$$\Omega_{n_z,\ell,q} \approx \Omega\langle n_z + \ell, q + \phi|\mathrm{e}^{i2\pi z/\lambda_{\mathrm{c}}}|n_z, q\rangle$$

are the Rabi frequencies and Ω is the 'bare' Rabi frequency. In the regime in which the tight-binding approximation is valid (that is, not very shallow lattices), $\Omega_{n_z,\ell,q}$ is a slowly varying function of q. On the other hand, it has a strong dependence on ℓ and for $|\ell| > 0$ is suppressed by the Lamb–Dicke parameter $\eta_{\mathrm{LD}} = k_{\mathrm{L}}\sqrt{\hbar/(2\omega_z m)}$,

resulting in an effective Rabi frequency for the first sidebands ($\ell = \pm 1$) that is approximately an order of magnitude below that of the carrier.

We have also introduced the Boltzmann factors

$$q_z(\ell_0, n_z, q) \equiv \exp\{-\beta_z[E_{n_z+\ell_0,0,0}(q) - E_{\ell_0,0,0}(0)]\}$$
$$q_r(\ell_0, n_z, n_r, \upsilon) \equiv \exp\left\{-\frac{\beta_r}{L}\sum_{q'}[E_{n_z+\ell_0,n_r,\upsilon}(q') - E_{n_z+\ell_0,0,0}(q')]\right\}$$

with $\beta_{z,r} = 1/k_B T_{z,r}$ and L the total number of lattice sites. $Z = \sum_{n_z,q,n_r,\upsilon} q_z(\ell_0, n_z, q) q_r(\ell_0, n_z, n_r, \upsilon)$ is the partition function.

There are three leading mechanisms that lead to broadening of the line shape. One arises from the thermal population of different quasi-momentum states combined with the finite momentum transfer by the probe laser when interrogating the clock states. This type of motion-induced broadening, which is a direct signature of the SOC mechanism, is the lattice analogue of Doppler broadening[21], generally discussed in the context of the spectra of free particles. For the lattice case, instead of plane waves carrying specific momentum, we need to think about Bloch waves described by two quantum numbers—the quasi-momentum and the band index. The second broadening mechanism is power broadening arising for strong Rabi pulses. For our spectroscopic parameters, only the carrier transition is affected by this mechanism. The third source of broadening is the coupling between the radial and axial degrees of freedom, and so is strongly determined by the trapping frequencies and radial temperature. At short probing times (less than π pulses), this type of broadening in the carrier transition can be characterized by using a temperature-dependent tunnelling rate, as we explain below. For the sidebands, axial–radial coupling is the leading broadening mechanism[20], and it has been shown that this mechanism is well captured by the perturbative approach.

However, the first-order perturbative approach neglects the radial dependence of the Rabi frequencies and radial sideband transitions induced by the laser. As discussed in detail in ref. 20, the omitted higher-order terms can lead to a dephasing of the coherent oscillations in $P_\ell^\pm$ at long times compared to a π pulse and induce additional broadening of the sideband spectra. Nevertheless, those effects can be accounted for by using an effective radial temperature, which we used as an effective fitting parameter, and by performing a time-average of equation (5) for the case of long probe times:

$$\overline{P}_\ell^\pm = \frac{1}{2}\sum_{n_z,n_r,\upsilon,q} \frac{q_z(\ell_0, n_z, q) q_r(\ell_0, n_z, n_r, \upsilon)}{Z} \left|\frac{\Omega_{n_z',\ell,q}}{\Omega^{\pm\mathrm{eff}}_{n_z',\ell,q,n_r,\upsilon}}\right|^2 \quad (6)$$

The clock spectroscopy shown in Fig. 1c was taken by applying the clock laser at high power ($\Omega = 2\pi \times 200$ Hz) and for many Rabi periods (during 80 ms), and so we used equation (6) to model the experiment and treated the radial temperature as a fitting parameter. The radial temperatures that provided the best fit varied between 7 μK and 9 μK and so were higher than the radial temperatures measured experimentally through motional spectroscopy of the sidebands, consistent with previous detailed studies of the sideband line shapes[20].

For the carrier transition, the dominant decoherence mechanism arising from radial sideband transitions manifests at long probing times as dephasing. This effect is shown in Extended Data Fig. 2, where it can be seen that the perturbative model (equation (5) with $\ell = 0$) does an excellent job for pulses shorter than a π pulse. However, for the longer pulse used (Extended Data Fig. 2e), the perturbative theory captures only the width of the line shape and not its amplitude.

Theoretical fit function to extract the VHS splittings. The coupling between the radial and axial degrees of freedom can be accounted for in the carrier line shape by defining an effective thermally averaged tunnelling rate. In the regime in which the tight-binding approximation is valid,

$$\langle \Delta E_{n_z,n_r,\upsilon}(q)\rangle \equiv \langle E_{n_z,n_r,\upsilon}(q+\phi) - E_{n_z,n_r,\upsilon}(q)\rangle$$
$$\approx -2\hbar J_{n_z}^{T_r}[\cos(q+\phi) - \cos(q)]$$

where $\langle\cdot\rangle$ denotes radial thermal averaging, and n_r and υ the radial and azimuthal harmonic oscillator mode numbers. Therefore, we can replace the effective Rabi coupling $\Omega^{\pm\mathrm{eff}}_{n_z,\ell,q,\upsilon}$ for the carrier ($\ell = 0$):

$$\Omega^{\pm\mathrm{eff}}_{n_z,0,q,n_r,\upsilon} \to \Omega^{\pm\mathrm{eff}}_{n_z}(q) = \sqrt{\Omega^2_{n_z,0,q} + [\pm\delta + 4J_{n_z}^{T_r}\sin(\phi/2)\,\sin(\phi/2+q)]^2}$$

where $J_{n_z}^{T_r}$ is the thermally averaged tunnelling rate and $\Omega_{n_z,\ell,q}$ is the Rabi coupling for the ℓth axial sideband. Even when the tight-binding approximation no longer holds, we can reproduce the VHS splittings by matching the thermally averaged bandwidth, computed from the analytic expression for the perturbative energies given above, to the tight-binding expression:

$$\max_q\langle\Delta E_{n_z,n_r,\upsilon}(q)\rangle - \min_q\langle\Delta E_{n_z,n_r,\upsilon}(q)\rangle = 8\hbar J_{n_z}^{T_r}\sin(\phi/2)$$

This expression, together with the approximation that all atoms are initially in the $\ell_0 = 0, 1$ band and that $\hbar J_{\ell_0}^{T_r} \ll k_B T_z$, is used to fit the carrier line shapes shown in Fig. 2, by convolving the resulting Rabi line shape with the joint transition density of states $\mathcal{D}_{\ell_0,T_r}$:

$$\overline{P}_0^\pm \approx \frac{1}{4\pi}\int_{-\pi}^{\pi}\left|\frac{\Omega_{\ell_0,0,0}}{\Omega^{\pm\mathrm{eff}}_{\ell_0}(q)}\right|^2 \mathrm{d}q = \frac{1}{2}\int_{-|4J_{\ell_0}^{T_r}\sin(\phi/2)|}^{|4J_{\ell_0}^{T_r}\sin(\phi/2)|} \mathcal{D}_{\ell_0,T_r}(\epsilon)\frac{\Omega^2_{\ell_0,0,0}}{\Omega^2_{\ell_0,0,0} + (\pm\delta - \epsilon)^2}\mathrm{d}\epsilon$$

where

$$\mathcal{D}_{\ell_0,T_r}(\epsilon) = \begin{cases} \dfrac{1}{\sqrt{\left[4J_{\ell_0}^{T_r}\sin(\phi/2)\right]^2 - \epsilon^2}} & -\left|4J_{\ell_0}^{T_r}\sin(\phi/2)\right| \le \epsilon \le \left|4J_{\ell_0}^{T_r}\sin(\phi/2)\right| \\ 0 & \text{otherwise} \end{cases}$$

When fitting this function to the split line data of the type shown in Fig. 2a, b to extract the VHS splitting plotted in Fig. 2c, the only free parameters used are a single parameter for the thermally averaged tunnel coupling J and an additional parameter for the amplitude of the split line. The amplitude is required as a free parameter only when a pulse longer than a single π pulse is used to increase the excitation fraction. The no-free-parameter theory predictions plotted in Fig. 2c were generated by applying the perturbative model to measured spectra of the motional sidebands at each axial trapping potential. As mentioned above, the radial temperatures used for the perturbative model varied between 7 μK and 9 μK.

Chiral Bloch vector dynamics. To model the chiral Bloch vector dynamics, the Rabi oscillations measured after preparing the atoms within a window of quasi-momenta centred around q^* and with width Δq are expressed as

$$\overline{P}_0^+(q^*) = \frac{1}{\Delta q}\sum_{q\in\Delta q}\left|\frac{\Omega_{0,0,0}}{\Omega_0^{+\mathrm{eff}}(q^* + q - \Delta_{q/2})}\right|^2 \sin^2\left[\frac{t}{2}\Omega_0^{+\mathrm{eff}}(q^* + q - \Delta_{q/2})\right]$$

To model the window, we simulate the atom preparation using a π pulse ($\Omega = 2\pi \times 10$ Hz) with five different initial pulse detunings δ^*. Because the Rabi frequency and tunnelling rates are comparable, the window is relatively broad, resulting in dephasing of the quasi-momentum-dependent Rabi oscillations shown in Fig. 4d when a second, stronger Rabi pulse is applied. Extended Data Fig. 3 shows the expected quasi-momentum distributions. Additionally, for the theoretical lines presented in Fig. 4, we set $\Delta = 4J_{\ell_0}^{T_r}\sin(\phi/2) = 2\pi \times 67\ \mathrm{s}^{-1}$ and $\Delta q \approx \pi\hbar/a$.

Data availability. The data supporting the findings of this study are available within the paper and its Extended Data.

30. Lignier, H. *et al.* Dynamical control of matter-wave tunnelling in periodic potentials. *Phys. Rev. Lett.* **99,** 220403 (2007).
31. Parker, C. V., Ha, L.-C. & Chin, C. Direct observation of effective ferromagnetic domains of cold atoms in a shaken optical lattice. *Nat. Phys.* **9,** 769–774 (2013).
32. Jotzu, G. *et al.* Experimental realization of the topological Haldane model with ultracold fermions. *Nature* **515,** 237–240 (2014).
33. Fläschner, N. *et al.* Experimental reconstruction of the Berry curvature in a Floquet Bloch band. *Science* **352,** 1091–1094 (2016).
34. Müller, T., Fölling, S., Widera, A. & Bloch, I. State preparation and dynamics of ultracold atoms in higher lattice orbitals. *Phys. Rev. Lett.* **99,** 200405 (2007).
35. Spielman, I. B. *et al.* Collisional deexcitation in a quasi-two-dimensional degenerate bosonic gas. *Phys. Rev. A* **73,** 020702 (2006).
36. Bishof, M. *et al.* Inelastic collisions and density-dependent excitation suppression in a ^{87}Sr optical lattice clock. *Phys. Rev. A* **84,** 052716 (2011).
37. Martin, M. J. *Quantum Metrology and Many-body Physics: Pushing the Frontier of the Optical Lattice Clock.* PhD thesis, Univ. Colorado, Boulder (2013).
38. Wall, M. L., Hazzard, K. R. A. & Rey, A. M. Effective many-body parameters for atoms in nonseperable Gaussian optical potentials. *Phys. Rev. A* **92,** 013610 (2015).

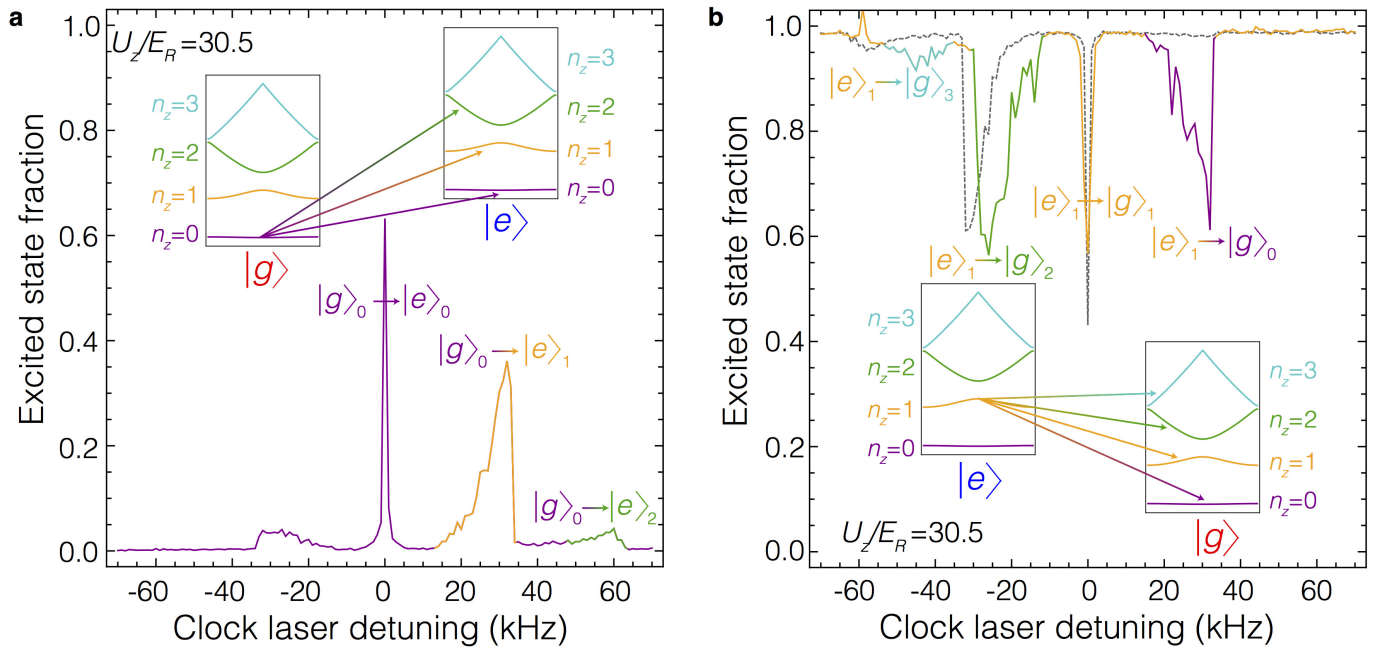

Extended Data Figure 1 | Bloch band preparation and spectroscopy. a, Spectroscopy of atoms prepared in $|g\rangle_0$ reveals the band spacing of the lattice, with inter-band transitions colour-coded by the final band. **b**, Spectroscopy of atoms in $|e\rangle_1$, prepared by driving the $|g\rangle_0 \rightarrow |e\rangle_1$ transition shown in **a** and then removing any remaining atoms in $|g\rangle$. The spectrum for atoms in $|e\rangle_0$ from Fig. 1d is shown for comparison (dashed grey line).

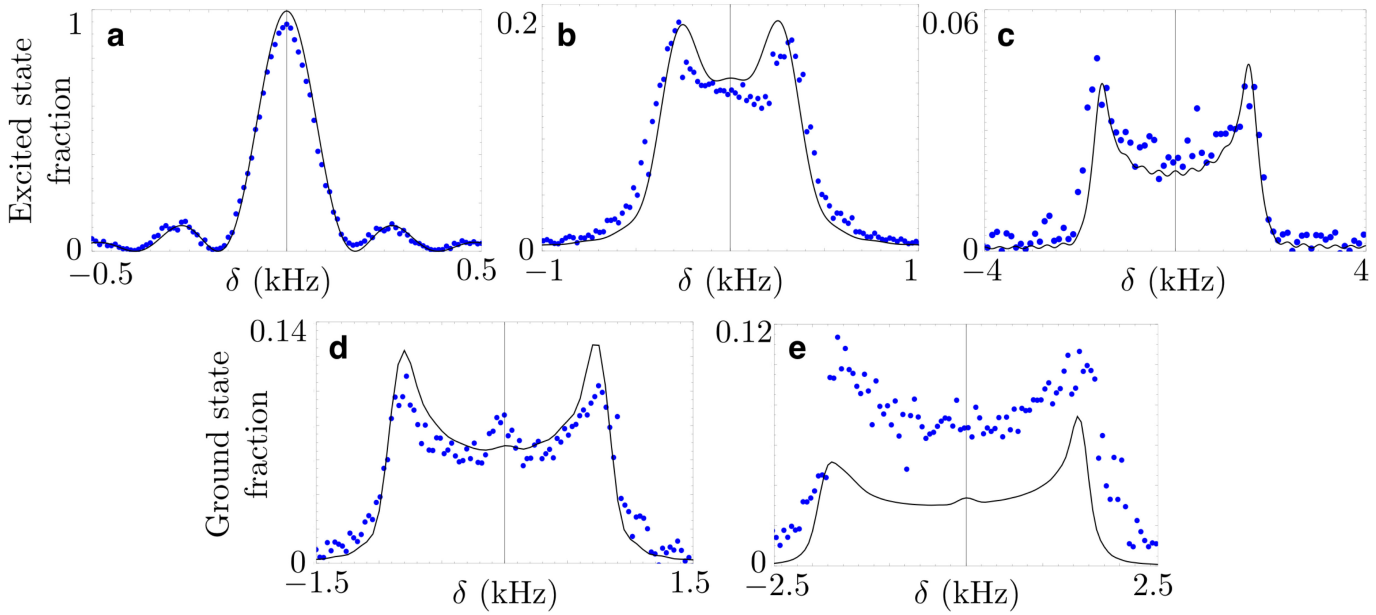

Extended Data Figure 2 | Rabi line shape modelling. a–e, Theoretical modelling of carrier line shapes starting from the $|g\rangle_0$ (**a**–**c**) or $|e\rangle_1$ (**d**, **e**) state. For the ground band transitions (**a**–**c**), all data were taken using a π pulse, and are well reproduced by a perturbative model (solid lines). Three specific cases are shown covering from the deep-lattice regime ($U_z \approx 65E_r$; **a**) to the moderate-lattice regime ($U_z \approx 10E_r$; **b**), and down to the shallow-lattice limit ($U_z \approx 3E_r$; **c**). For the first excited band transitions, the data in the deeper-lattice case ($U_z \approx 21.3E_r$), taken with a π pulse, are well reproduced by the perturbative model (**d**). However, for the case of $U_z \approx 16E_r$ where a longer pulse was used, the perturbative theory, which ignores radial sideband transitions induced by the laser, captures only the width of the line shape and not its amplitude (**e**).

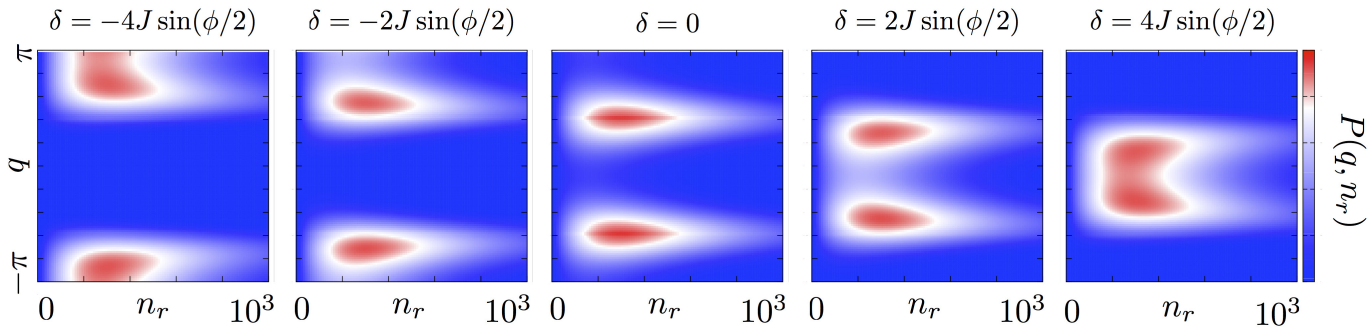

Extended Data Figure 3 | Modelling of quasi-momentum selection. Theoretical probability distribution $P(q, \boldsymbol{n}_r)$ of quasi-momentum and radial quantum number $\boldsymbol{n}_r$ of $|e\rangle$ excitations resulting from exciting a thermal distribution in $|g\rangle$ with a 50-ms π pulse. The lattice depth is $U_z \approx 16E_r$, resulting in a tunnelling rate of $J \approx 17$ Hz. The distribution of atoms among q is broadened owing to the fact that the Rabi frequency and tunnelling rates are comparable, but can be made narrower by decreasing the Rabi frequency.